minerals

MDPI

Article

Textures and Chemical Compositions of Magnetite from Zhibo Submarine Volcanic Iron Oxide Deposit, Xinjiang, China: Implications for Re-Equilibration Processes

Yang Wu [1,2,3], Ping Shen [1,2,3], Haoxuan Feng [1,2,*], Changhao Li [1,2,*], Jiayu Zhao [1,2,3], Yaoqing Luo [1,2,3] and Wenguang Li [1,2,3]

[1] Key Laboratory of Mineral Resources, Institute of Geology and Geophysics, Chinese Academy of Sciences, Beijing 100029, China; wuyangcz@163.com (Y.W.); pshen@mail.iggcas.ac.cn (P.S.)
[2] Innovation Academy for Earth Science, Chinese Academy of Sciences, Beijing 100029, China
[3] College of Earth and Planetary Sciences, University of Chinese Academy of Sciences, Beijing 100049, China
* Correspondence: hxfeng@mail.iggcas.ac.cn (H.F.); lch61522191@mail.iggcas.ac.cn (C.L.)

Abstract: The Awulale Iron Metallogenic Belt (AIMB) has developed many medium–large iron deposits, of which the Zhibo iron deposit is selected as the research object in this paper. The Zhibo deposit's ore primarily consists of magnetite as the main mineral, accompanied by extensive epidotization. The mineral assemblage includes diopside, albite, actinolite, epidote, chlorite, K-feldspar, quartz, calcite, chalcopyrite, and pyrite. Magnetite is classified into two groups based on sulfide content and mineral assemblage (MagI for sulfide-free and MagII for sulfide-rich ores). Two-stage mineralization of magnetite has been identified based on mineral assemblages and paragenesis, including the magmatic stage MagI and hydrothermal stage MagII. Mag I shows inhomogeneous backscattered electron (BSE) textures and consists of BSE-light and -dark domains (Mag I-L and MagI-D). Seven subtypes of magnetite have been recognized in this deposit. MagI-L and MagI-D have formed in the magmatic stage and show BSE images in light and dark colors, respectively. MagI-L is anhedral to subhedral and is inclusion-free. MagI-D has mainly replaced MagI-L along fractures and contains inclusions and pores. MagII has formed in the hydrothermal stage and is characterized by coupled dissolution–reprecipitation (DRP) textures. It can be divided into five subgenerations, that is, MagII-1, MagII-2, MagII-3, MagII-L, and MagII-D. MagII-1, MagII-2, and MagII-3 comprise the core–mantle–rim texture, while MagII-L and MagII-D comprise the core–rim texture. MagII-1 is BSE-light and is enriched with inclusions and pores. MagII-2 has partly replaced MagII-1 and exhibits oscillatory zoning under BSE imaging. It also contains inclusions. BSE-light MagII-3 occurs as overgrowth along MagII-2 margins and is inclusion-free. MagI magnetite is enriched with V, Cr, and Ni, whereas MagII is enriched with W, Ta, Nb, Sr, Sb, Sn, Y, Zr, Mg, Al, and Ti, indicating a decreased temperature of magnetite formation. MagI-L crystallizes from the original magma, while MagI-D is formed from the residual magma enriched with incompatible elements. MagII crystallizes from later multiple hydrothermal activities through the dissolution of early magnetite and the re-precipitation of later magnetite or from MagI-D which has later undergone a hydrothermal overprinting process. According to the texture and chemical composition of magnetite from the Zhibo deposit, we suggest that the Zhibo iron deposit was formed from the initial magmatic origin and then underwent a hydrothermal overprinting process.

Keywords: magnetite; texture and mineral composition; Zhibo deposit; western Tianshan

Citation: Wu, Y.; Shen, P.; Feng, H.; Li, C.; Zhao, J.; Luo, Y.; Li, W. Textures and Chemical Compositions of Magnetite from Zhibo Submarine Volcanic Iron Oxide Deposit, Xinjiang, China: Implications for Re-Equilibration Processes. *Minerals* **2024**, *14*, 548. https://doi.org/10.3390/min14060548

Academic Editor: Lluís Casas

Received: 30 March 2024
Revised: 21 May 2024
Accepted: 22 May 2024
Published: 26 May 2024

1. Introduction

The western Tianshan metallogenic belt in Xinjiang is an important part of the Central Asia Orogenic Belt (CAOB) and hosts many iron, copper, gold, and other metal–mineral resources related to the tectonic evolution of multiple accretionary orogens [1–6].

Submarine volcanogenic iron oxide (SVIO) deposits constitute the primary deposit type within the Awulale Iron Metallogenic Belt (AIMB) located in the western Tianshan metallogenic belt (Figure 1a,b). These deposits are characterized by medium to large-sized occurrences, including Shikebutai, Songhu, Chagangnuoer, Zhibo, Dunde, and Beizhan deposits, arranged from west to east (Figure 1b) [7].

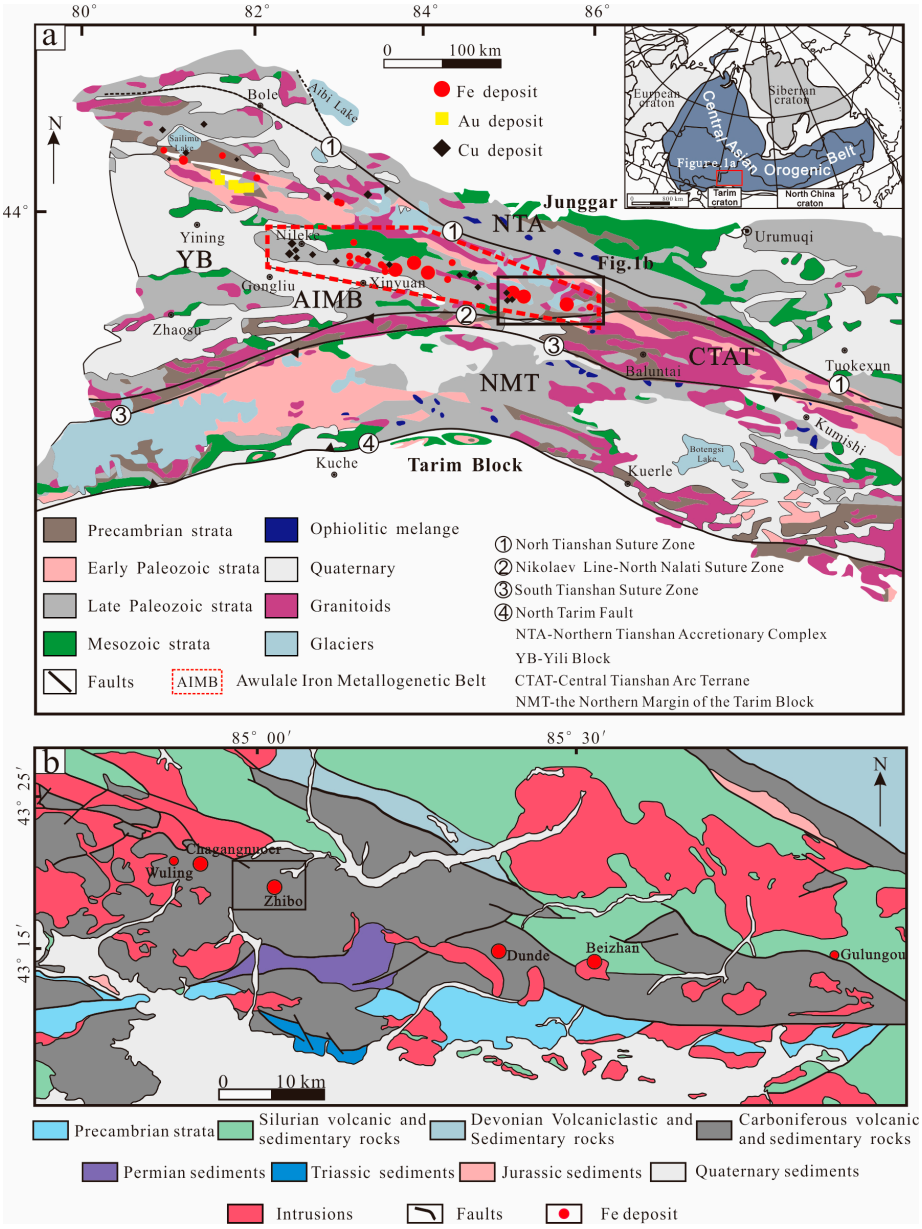

Figure 1. Geological maps of (**a**) the western Tianshan metallogenic belt (modified from [8]) and (**b**) the eastern part of the AIMB (modified from [9]).

The iron deposits within the AIMB are mainly hosted in Late Palaeozoic submarine calc-alkaline volcanic–subvolcanic and volcano-sedimentary rocks [10–15]. The formation of these deposits is related to a transition in genesis from magmatic and hydrothermal to sedimentary mineralization, depending on the distance from the volcanic center or core [1,5,16].

The Zhibo iron deposit is one of the largest submarine volcanic iron deposits in the AIMB. The field observations made in the Zhibo iron deposit are similar to those found in iron oxide–apatite (IOA) or Kiruna-type, suggesting that the ore deposit has a magmatic origin [12,17–21]. The characteristics comprise clearly defined contact between the ore and

the host rock, a simplified mineral assemblage, the presence of high-grade ores, and structurally controlled ore veins [12,22]. There are two major groups of magnetite based on the ore textures, mineral associations, and elemental and isotopic composition of magnetite. The first group, enriched with Ti, V, Ni, and HFSE, resembles iron oxide–copper–gold (IOCG) ores [22]. The iron and oxygen isotope investigations of this magnetite reveal that the Zhibo iron deposit has a magmatic origin. The second group is depleted in Ti, V, Ni, and Y, with a wider range in δ^{56}Fe and δ^{18}O, resembling hydrothermal Fe–skarn ores [20–27]. Therefore, the origin of the Zhibo deposit remains controversial. The mineralization process can readily alter the texture and composition of magnetite. Inadequate previous research on the texture of magnetite in the Zhibo deposit has contributed to controversies surrounding the deposit genesis [10,12,28].

Magnetite, a prevalent oxide mineral, not only occurs in sedimentary, metamorphic, and magmatic rocks as an accessory mineral [29–33], but also is extensively distributed as a major or trace mineral in various types of mineral deposits [34]. Magnetite encompasses numerous minor and trace elements, the concentrations of which may be affected by the diverse range of physicochemical conditions encountered during formation in different mineral deposits [35,36]. Hence, magnetite finds broad applications as a petrogenetic indicator and pathfinder mineral for mineral exploration [31,37,38]. By compiling the composition of magnetite in various deposits, a series of discriminant diagrams have been established to identify different types of mineral deposits [31,34,37,39–41]. Numerous detailed texture studies on magnetite have been extensively employed in the investigation of IOA, IOCG, and skarn deposits. Variations in magnetite textures and compositions at different stages are used to trace the fluid evolution process and the genesis of the deposit [18,42–45].

In this paper, we conduct detailed investigations on the textures and compositions of magnetite from the Zhibo deposit. Based on these results, we discuss the genesis of the Zhibo deposit. The findings of this study are of significant importance in understanding the origin of iron ore deposits hosted in volcanic–subvolcanic rocks.

2. Geological Setting

2.1. Geology of Western Tianshan

Located on the southwestern edge of the Central Asian Orogen Belt (CAOB), the Western Tianshan Orogen is situated between the Junggar terrane to the north and the Tarim block to the south (Figure 1a). It comprises the Northern Tianshan Accretionary (NTA), the Yili Block (YB), the Central Tianshan Arc Terrane (CTAT), and the Northern Margin of the Tarim Block (NMT). These are separated by the North Tianshan Suture Zone (NTSZ), the Nikolaev Line–North Nalati Suture Zone (NNSZ), and the South Tianshan Suture Zone (STSZ) from north to south (Figure 1a) [8,10,12,46–48]. Previous studies have suggested that the suture zones are linked to the subduction of the Late Palaeozoic North Tianshan, Early Palaeozoic Terskey, and the latest Early Palaeozoic–Late Palaeozoic South Tianshan oceans during Early Palaeozoic to Early Mesozoic times [5,8,12,49]. The dominant strata in the Western Tianshan Orogen consist of Precambrian metamorphic basement rocks, Palaeozoic sedimentary, and volcanic rocks [2]. The zircon U-Pb ages of the Precambrian metamorphic basement vary from 1910 Ma to 882 Ma [50].

The Awulale Iron Metallogenic Belt (AIMB) is situated to the east of the Yili Block (Figure 1b), and the strata are mainly composed of Precambrian basement and Late Paleozoic and Mesozoic rocks [51,52]. The Precambrian basement includes granitic gneisses, migmatites, schists, and amphibole monzogneiss, predominantly found in the southern AIMB (Figure 1b) [53,54]. Silurian rocks in the northeastern AIMB comprise metamorphic and clastic formations, such as siltstone, metamorphic conglomerate, tuff, sandstone, and schist. The NNW-SE trending Devonian rocks are primarily composed of pyroclastic rocks, acid volcanic rocks, and carbonates.

The Carboniferous strata consist of intermediate-acid volcanic–sedimentary clastic rocks belonging to the Dahalajunshan Formation. These rocks encompass calc-alkaline

basalts, trachy andesites, trachy andesites with subordinate basalts, rhyolites, and volcaniclastic rocks. The U-Pb zircon ages of basalts, basaltic andesite, trachyte–andesite, and rhyolites range from 361 Ma to 316 Ma [2].

The Dahalajunshan Formation is the primary host rock for syngenetic submarine volcanogenic iron oxide deposits [2,28]. Multiple tectonic episodes provide the driving force for the activation and migration of endogenous mineral ore-forming materials. Additionally, geological structures serve as conduits for fluid activity and sedimentation. The WNW-trending structure and north-dipping high-angle faults in the AIMB are well developed [55]. The major iron deposits in the AIMB are controlled by the Carboniferous volcanic apparatus, with the Zhibo iron deposit situated in the center of the caldera structure [1]. Circular and radial faults play crucial roles as key ore-controlling structures and host iron orebodies.

2.2. Geology of the Zhibo Iron Ore Deposit

The Zhibo iron deposit (Figure 2a) is a significant iron deposit situated in the eastern part of the AIMB, boasting an iron ore resource exceeding 250 million tons, with an average grade exceeding 40%. The Zhibo iron mine is about 5.5 km long and 1.5 km wide (Figure 2a), and it is divided into three mining areas: eastern, middle, and western, of which the east is the principal mining area. The Zhibo deposit comprises more than 21 ore bodies which are massive, tabular, and lenticular (Figure 2b,c). The Fe8 ore bodies on the C-C ‘section line are tabular and lenticular, sub-horizontally distributed, and reach more than 80 m in length (Figure 2c).

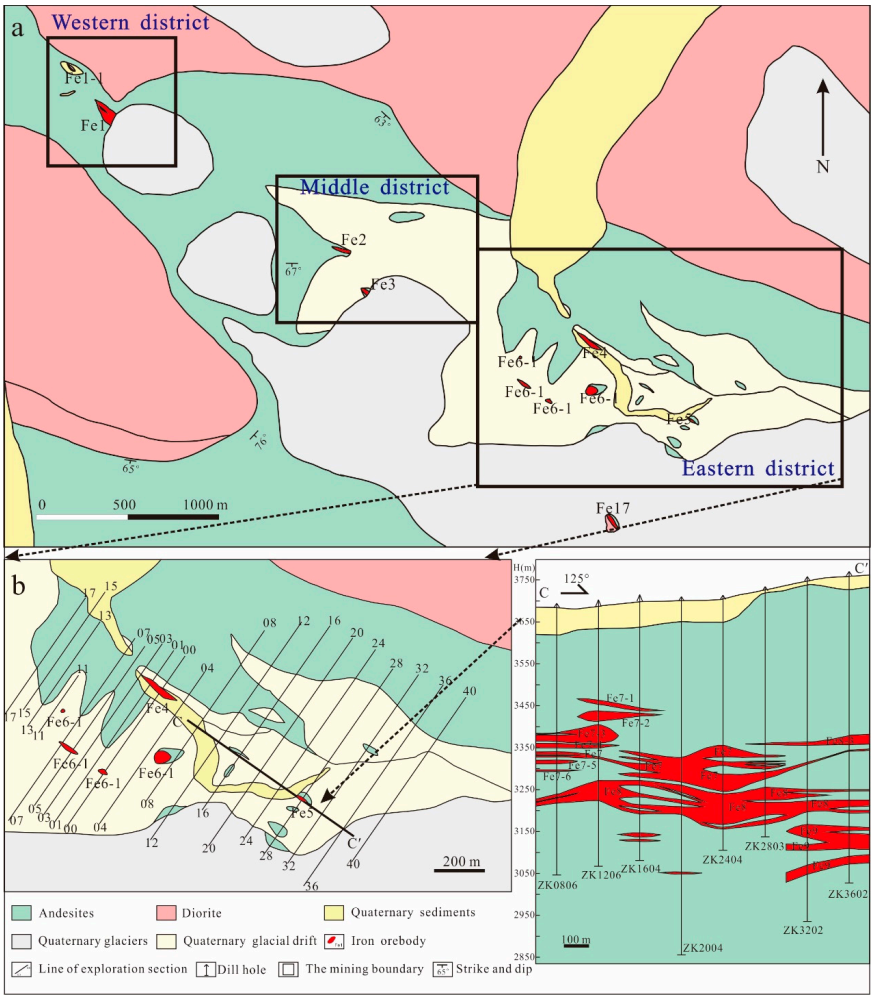

Figure 2. A geological map of (**a**) the Zhibo iron deposit, (**b**) the eastern mining section, and (**c**) simplified geological sections along the C-C′ line (the figures are modified from [56]).

The exposed strata in the mine are characterized by the Carboniferous Dahalajunshan Formation, which mainly consists of basalt, basaltic tuff, basaltic trachyte–andesite, trachyte–andesite, and andesite (Figure 2). The iron orebodies are primarily hosted within the basaltic andesite and andesite (Figure 2c). This basaltic andesite typically appears gray or greyish–green and contains phenocrysts of plagioclase (20~25 vol%) and clinopyroxene (10–15 vol%) (Figure 3a,b). The matrix of andesite comprises fine plagioclase, clinopyroxene, and amphibole. The plagioclase phenocrysts are euhedral–subhedral, with a particle size of around 0.2–0.5 mm. Clinopyroxene phenocrysts that have been partially replaced by epidote also display euhedral–subhedral morphology. Moreover, andesite contains magnetite which serves as an accessory mineral (Figure 3d–g).

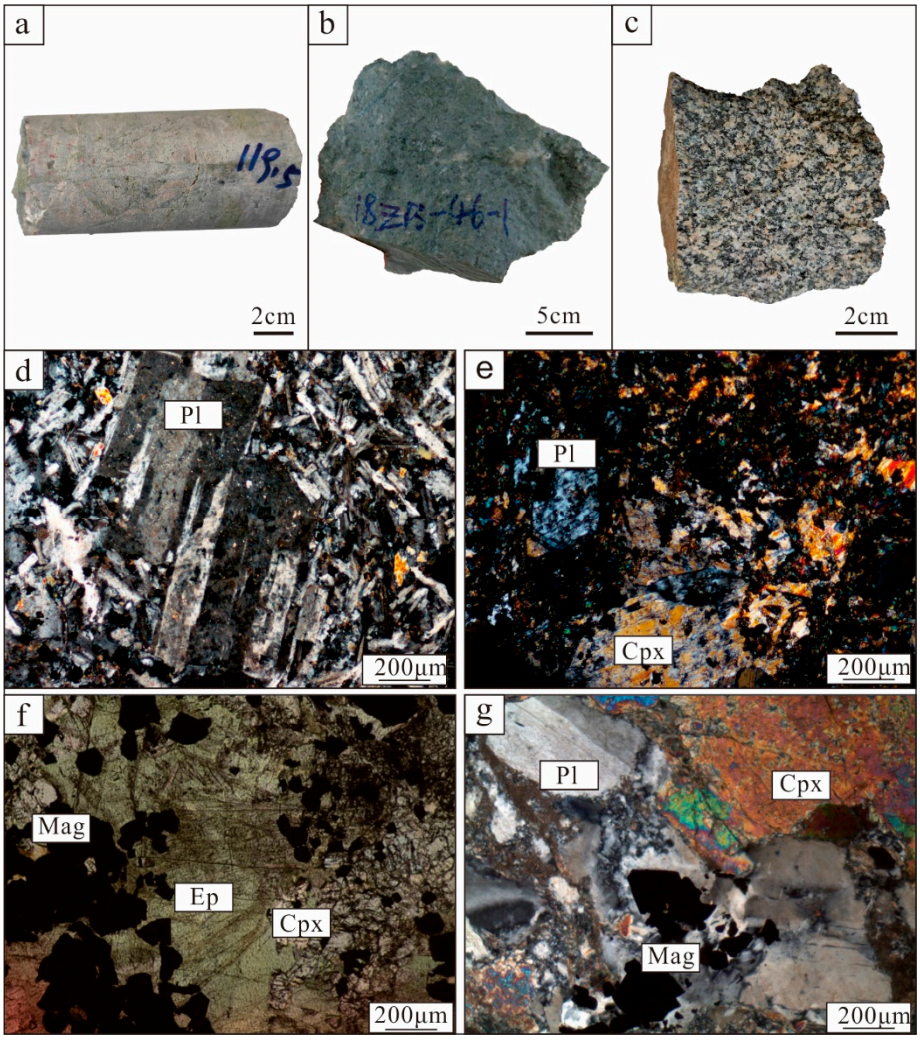

Figure 3. Hand specimens and photomicrographs of wall rocks from Zhibo deposit. (**a**) Gray andesite is located in upper part of orebodies. (**b**) Grey–green andesite containing plagioclase phenocrysts. (**c**) Hand sample of granodiorite. (**d**) Plagioclase phenocrysts in andesite (cross-polarized light). (**e**) Andesite contains plagioclase and clinopyroxene phenocrysts (cross-polarized light). (**f**) Clinopyroxene replaced by epidote and magnetite is present in andesite (plane-polarized light). (**g**) Plagioclase and clinopyroxene phenocrysts and magnetite are present in andesite, accompanying epidotization alteration (cross-polarized light). Mag = magnetite; Pl = plagioclase; Ep = epidote; Cpx = clinopyroxene.

The host andesite is exposed in the central and southern areas where it strikes NW, with a steep dip angle (50~75°) near the surface and a shallower dip angle (10~30°) at deeper levels. Previous studies have indicated that the formation age of the Dahalajunshan Formation is >361~313 Ma [2]. The intrusive rocks include granodiorite in the

southwestern area and quartz diorite in the northern area (Figures 2a and 3c). The diorite and granite have U-Pb ages of 318.9 ± 1.5 Ma and 304.1 ± 1.8 Ma, respectively [9,57]. The igneous zircon U-Pb ages of the Zhibo andesite and disseminated ore are 328.7 ± 2.1 Ma and 329.9 ± 1.5 Ma, respectively [28]. In situ U-Pb dating of titanite in the ore was used to constrain the time of iron mineralization and yielded three ages of 310.3 ± 1.8 Ma, 310.1 ± 1.8 Ma, and 315.3 ± 2.5 Ma [57]. In conclusion, it is generally believed that the main metallogenic age in the Zhibo deposit is not earlier than 330 Ma.

2.3. Ore Types and Paragenetic Sequence

The boundary between the orebody and wall rock exhibits primarily a gradual relationship (Figure 4a), occasionally displaying a sharp contact relationship (Figure 4b).

Several distinct ore types have been identified, characterized by their texture and mineral composition. These include massive (Figure 4c–e), disseminated (Figure 4f), breccia (Figure 4g,h), and banded types (Figure 4i), along with a minor occurrence of lava ores (Figure 4j).

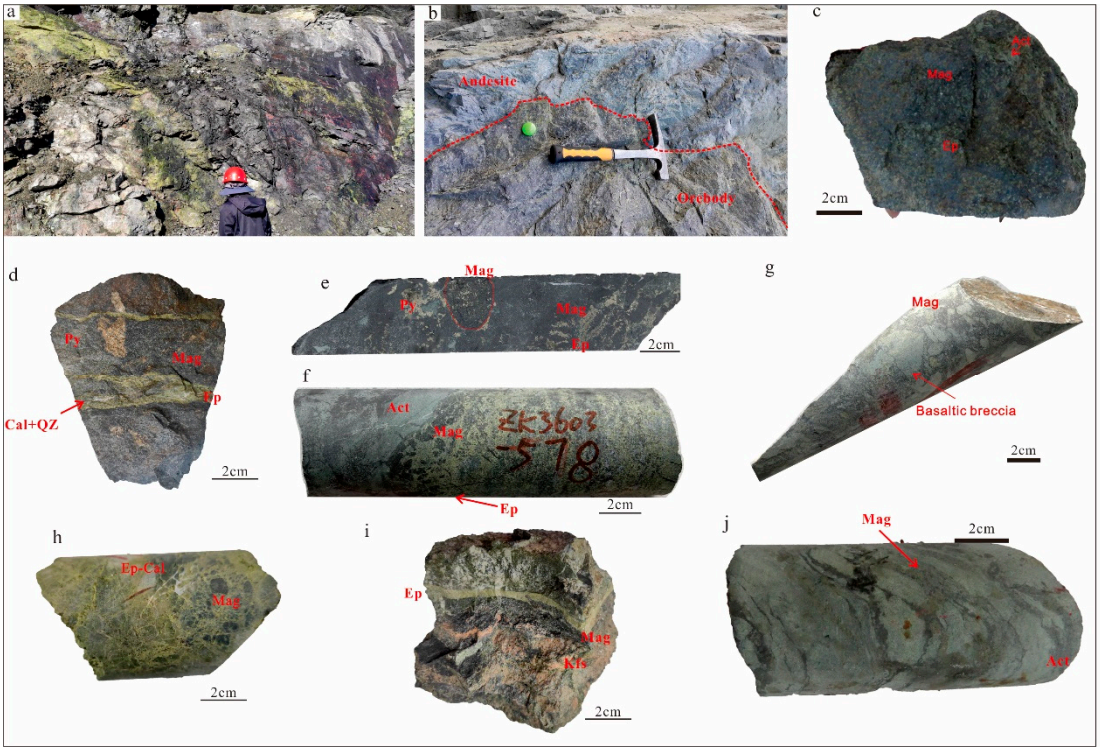

Figure 4. Photographs of outcrops and hand specimens from the Zhibo iron deposit. (**a**) The ore body is in contact with the epidote alteration; (**b**) a massive ore is intercalated with andesite; (**c**) a massive magnetite ore; (**d**) a massive magnetite ore crosscut by an epidote–quartz–calcite vein; (**e**) a massive magnetite ore with dendritic magnetite inclusions; (**f**) a disseminated magnetite ore; (**g**) a complex breccia magnetite ore; (**h**) a complex breccia magnetite ore; (**i**) a banded magnetite ore; and (**j**) magnetite lava with flow texture. Act = actinolite; Cal = calcite; Di = diopside; Ep = epidote; Mag = magnetite; Py = pyrite; Qz = quartz.

In the Zhibo deposits, high-grade massive ores can be classified into two types based on their mineral compositions. One type consists mainly of magnetite as the ore mineral, along with diopside, albite, and actinolite (Figure 4c). In this type of ore, magnetite predominates with subhedral to euhedral fine-grained aggregates (Figure 5a,b). The other type of ore not only contains massive aggregates of magnetite but also shows dendritic aggregates of magnetite, along with pyrite, chalcopyrite, and epidote (Figure 4d,e). Magnetite in this type of ore exhibits subhedral to euhedral crystals (Figure 5c), and platelet magnetite can be observed within dendritic magnetite aggregates (Figure 5d). Pyrite

mainly displays an anhedral to subhedral structure (Figure 5c,d). Brecciated magnetite ores come in two types. One variety of volcanic rock breccias is identified by the presence of magnetite as the cementing matrix (Figure 4g). The other type is characterized by epidote cement and magnetite fragments (Figure 4h). The banded magnetite ores consist of a layer of magnetite, K-feldspar, and epidote, which are intersected by minerals resulting from late alterations (Figures 4i and 5e). Disseminated magnetite ores are characterized by magnetite distributed within an epidote–chlorite–K-feldspar–chlorite matrix (Figure 5f).

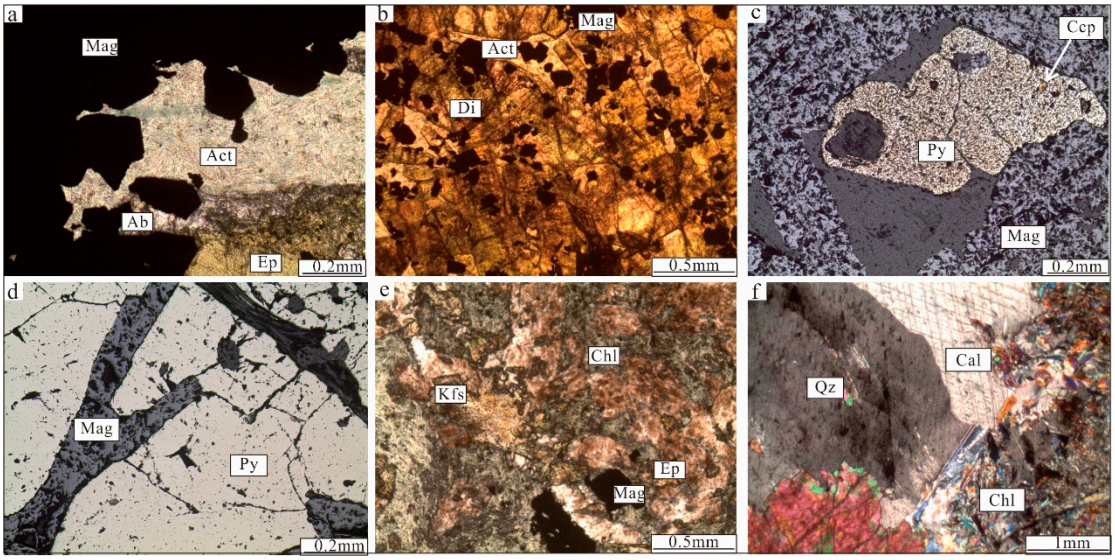

Figure 5. Photomicrographs from the Zhibo iron deposit. (**a**) Euhedral magnetite, with actinolite and albite filling the interstices between the magnetite crystals (plane-polarized light); (**b**) volcanic rock is replaced by an alteration assemblage of diopside and albite, with magnetite (plane-polarized light); (**c**) pyrite replaces magnetite (reflected light); (**d**) platy magnetite with granules of pyrite (reflected light); (**e**) subhedral magnetite grows with K-feldspar, epidote, and chlorite; (**f**) calcite is associated with quartz and chlorite (cross-polarized light). Ab = albite; Act = actinolite; Cal = calcite; Ccp = chalcopyrite; Chl = chlorite; Di = diopside; Ep = epidote; Mag = magnetite; Py = pyrite; Qz = quartz.

The hydrothermal alteration of wall rocks encompasses sodic(–calcic) alteration (actinolite and albite), epidote± sulfide ±chlorite, and K-feldspar alteration.

Based on paragenesis, texture, and crosscutting relationships, the alteration and mineralization processes at Zhibo could be divided into four stages: (1) Na–Ca alteration stage, (2) K–Ca alteration stage, (3) epidote–sulfide stage, and (4) calcite–quartz stage (Figure 6). The Na–Ca alteration stage (Stage 1) comprises volcanic rocks and tuff diopside–albite alteration assemblages. The K-Ca alteration stage (Stage 2) is characterized by magnetite, actinote, and epidote. The epidote–sulfide alteration stage (Stage 3) is marked by the prevalence of magnetite, pyrite, epidote–potassium feldspar, (pyrrhotite), and (chalcopyrite). The calcite–quartz stage (Stage 4) exhibits a combination of quartz–calcite–chlorite–(hematite) and (pyrrhotite).

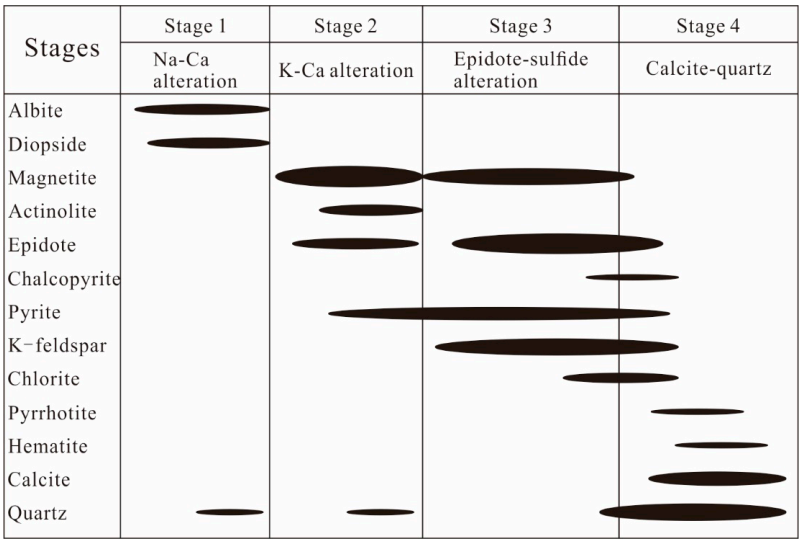

Figure 6. Paragenesis of minerals and alteration in the Zhibo iron deposit (The long axis of the black ellipse indicates the duration, while the short axis indicates the relative amount of mineral formation).

3. Sample and Method

In this study, magnetite samples exhibiting various types and mineral assemblages were carefully selected to conduct comprehensive investigations into their textural and mineral chemical characteristics. Specifically, five samples were collected from platform 3580 and drill ZK3602 located in the east mining area. Subsequently, three distinct types were subjected to further study, encompassing massive (18ZB45, 18ZB53-1, ZK3602-626), densely disseminated or semi-massive (ZK3602-629), and complex breccia (ZK3602-631) magnetite ores displaying different hydrothermal alteration signatures.

Backscattered electron (BSE) images and electron microprobe analysis (EMPA) were performed at the Institute of Geology and Geophysics, Chinese Academy of Sciences (IGGCAS). All samples were examined on carbon-coated thin sections within an evacuated chamber.

Japan JEOL Series Electronic Probe (JXA-8100 EMP) is the experimental facility used to analyze the components of major and trace elements of magnetite at an accelerating voltage of 15 kV, a beam current of 20 nA, a spot size of 2 μm, and a 10–30 s peak counting time. The following standards are used for calibration: diopside (Ca and Si), rutile (Ti), jadeite (Na and Al), garnet (Fe), bustamite (Mn), K-feldspar (K), pyrope (Mg), NiO (Ni), Cr_2O_3 (Cr), and V_2O_5 (V). The spectral line adopted by each element is Na (129.393nm), Mn (146.186nm), K (120.157nm), Mg (107.399 nm), Si (77.371 nm), Fe (134.625 nm), Al (90.551 nm), Ca (107.907 nm), Ti (88.751 nm), Cr (159.287 nm), V (174.129 nm), and Ni (115.165 nm), respectively. A program based on the ZAF procedure is used for data correction.

We chose the flat and clean magnetite under the microscope as the research object to reduce the impact of inclusions on the obtained experimental results. Magnetite trace element analyses were conducted by using LA-ICP-MS at the MNR Key Laboratory of Metallogeny and Mineral Assessment, Institute of Mineral Resources, CAGS. Laser sampling was performed using RESOlution S-155. A Bruker M90 ICP-MS instrument was used to acquire ion-signal intensities. Helium was applied as a carrier gas. Each analysis incorporated a background acquisition of approximately 15–20 s (gas blank) followed by 40–45 s of data acquisition from the sample. Element contents were calibrated against multiple reference materials (BCR-2G, BIR-1G, and GSE-1G) without applying internal standardization [58]. The preferred values of element concentrations for the USGS reference glasses are from the GeoReM database. Off-line selection and integration of background and

analyte signals, time drift correction, and quantitative calibration were performed by ICPMSDataCal-10.2 [58,59].

4. Results

4.1. Petrography and Texture of Magnetite

Two main stages of magnetite can be identified based on mineral assemblage and paragenesis. The first-stage magnetite, MagI, is magmatic in origin and occurs in sulfide-free ores, whereas the second-stage magnetite, MagII, is associated with hydrothermal sulfide-rich ores. The latter is further subdivided into five subtypes on the basis of ore types and BSE textures.

The massive ores are distinguished into sulfide-free ores (18ZB-45/18ZB-53) and sulfide-rich ores (ZK3602-626). Within the sulfide-free ores (18ZB-45/18ZB-53), two varieties of magnetite are observed, characterized as light and dark magnetite. MagI-L magnetite appears subhedral or euhedral and lacks inclusions (Figure 7a,b). In contrast, MagI-D magnetite, which replaces MagI-L magnetite along mineral fissures, typically contains inclusions and voids ranging from the faintly distributed micro- to nanometer scale (Figure 7a,b). The sulfide-rich ores (ZK3602-626) exhibit enriched subhedral sulfide (pyrite) and feature two types of magnetite. MagII-D, found near the contact point with pyrite, is dark and rich in inclusions, while MagII-L is relatively pure, bright magnetite without inclusions in the inner part of the magnetite along the cracks (Figure 7c). In terms of texture, some 120° triple junction textures are observed in the massive magnetite (MagII), indicating balanced crystallization (Figure 7d).

In samples ZK3602-629 and ZK3602-631, the magnetite manifests as platy magnetite. The magnetite in disseminated and breccia ores exhibits a more complex nature, with multiple generations of magnetite. MagII in samples (ZK3602-631/ZK3602-629) displays distinct characteristics of multi-stage formation. In sample ZK3602-629, magnetite with oscillatory zoning displays two types: MagII-L and MagII-D. MagII-D, characterized by its dark magnetite rich in inclusions and voids, has undergone replacement by MagII-L that grows in the boundary contact of MagII-D magnetite (Figure 7e).

The magnetite in dendritic ores (ZK3602-631) exhibits extremely complex core–mantle–rim textures. The core (MagII-1) consists of bright-colored magnetite rich in inclusions and voids. This core magnetite is subsequently replaced by the second-generation magnetite (MagII-2), characterized by alternating dark and light bands filled with irregular inclusions and voids (Figure 7f). The rim magnetite (MagII-3) develops along the second-generation light magnetite (MagII-2) and appears as pure magnetite with minimal inclusions and voids.

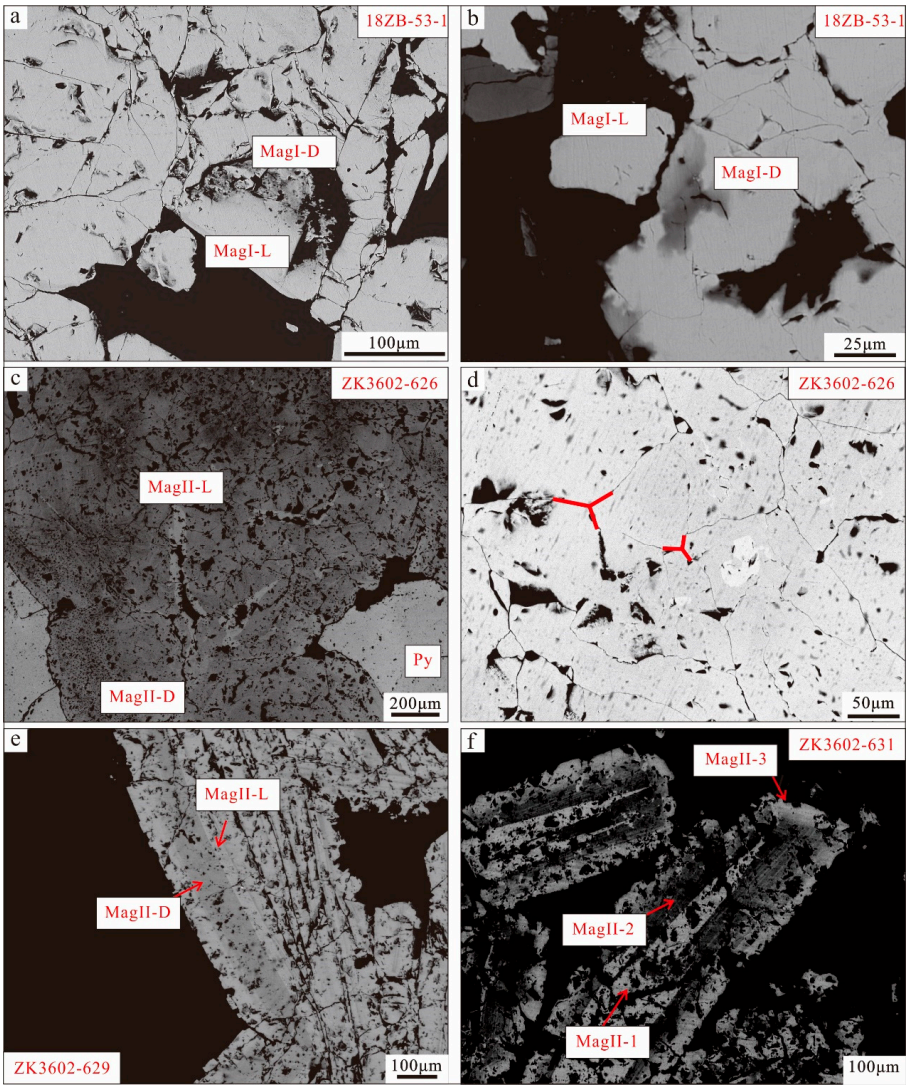

Figure 7. SEM-BSE images of magnetite. (**a**,**b**) MagI-L is subhedral–euhedral without inclusion. MagI-D replaces MagI-L magnetite along mineral fissures and contains inclusions and voids that vary from the faintly distributed micro- to nanometer scale; (**c**) MagII-D is dark magnetite with inclusion and voids which has been replaced by MagII-L, which grows in boundary integration contact of MagII-D magnetite; (**d**) fine-grained aggregated magnetite displays well-defined 120° triple junctions; (**e**) MagII-D with subhedral pyrite and MagII-L without inclusions; (**f**) core (MagII-1) is enriched with inclusions and voids. Core magnetite is replaced by MagII-2 with oscillatory zoning, and rim magnetite (MagII-3) grows along MagII-2.

4.2. Major Element Composition of Magnetite

The EMPA results of different types of magnetite are presented in Supplementary Table S1. The major elements are reported as oxides, including FeO and CaO (Figure 8). All magnetite samples exhibit relatively high SiO_2, MgO, Al_2O_3, and TiO_2 contents. Additionally, the MgO content is notably high across all samples. Other elements such as Na_2O, Cr_2O_3, K_2O, MnO, and V_2O_3 are either lower or slightly above their detection limits.

Throughout all stages of magnetite ore formation, dark magnetite generally displays higher and more variable SiO_2, CaO, MgO, and Al_2O_3 contents compared to light magnetite, whereas light magnetite tends to have higher FeO contents.

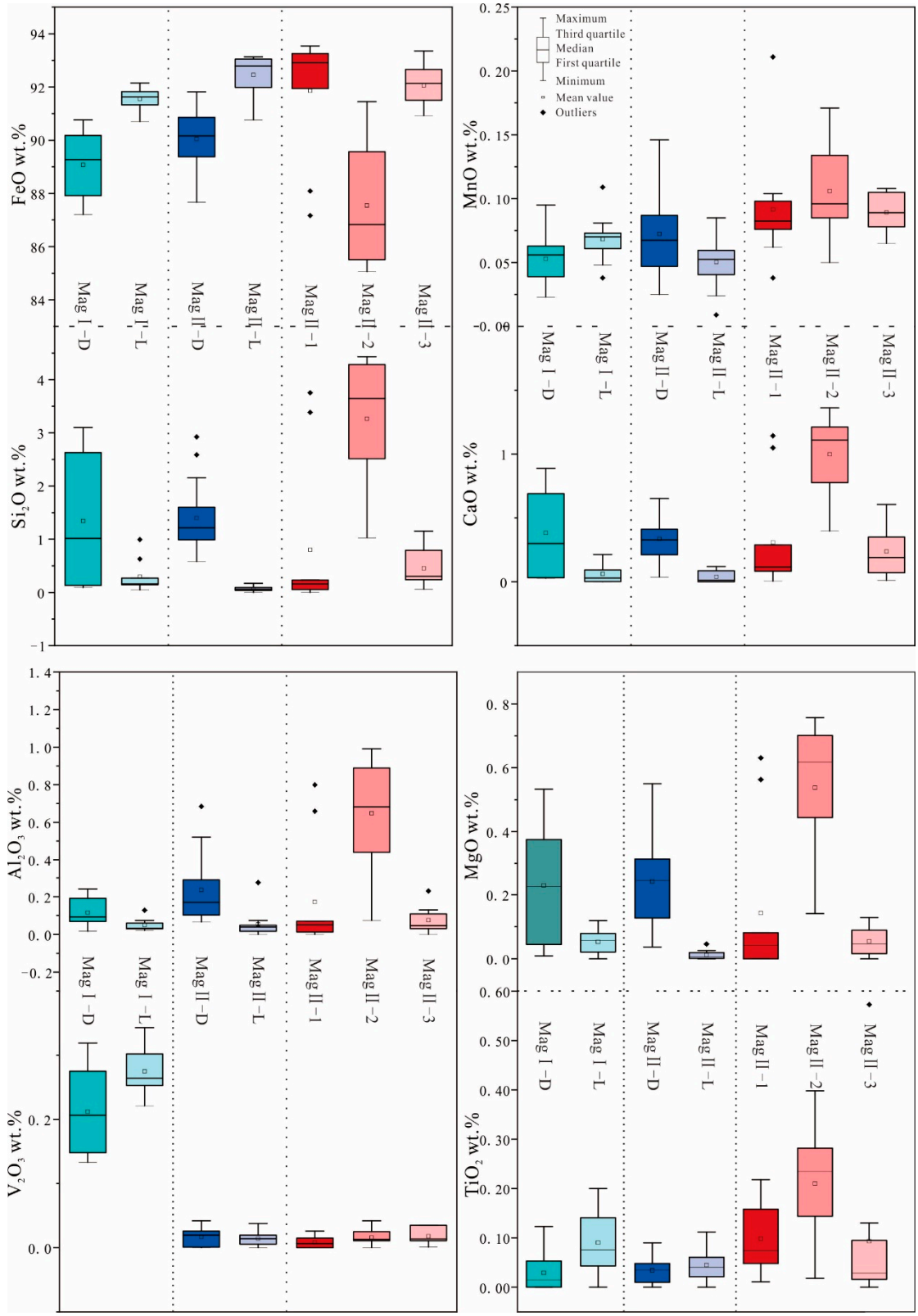

Figure 8. Box plots for magnetite EMPA.

The main feature of MagI is its high content of V_2O_3 (0.13–0.34 wt%), in which MagI-D (V_2O_3, 0.22–0.34 wt%) shows higher contents of V_2O_3 compared to MagI-L (V_2O_3, 0.13–0.321 wt%). MagI-L has fewer impurities and a higher FeO content. However, the contents of impurities in MagI-D fluctuate greatly; for example, the contents of SiO_2 (0.09–3.10 wt%), MgO (0.009–0.533 wt%), and CaO (0.03–0.89 wt%) have a large variance.

The composition variations among different subtypes of MagII are significant. The BSE-light magnetite (MagII-2) shows higher FeO contents than the BSE-dark magnetite (MagII-1 and MagII-3), which is similar to MagI. From MagII-1 to MagII-3, the contents of MnO, Al_2O_3, Si_2O, and CaO change in an inverted V shape. The composition change of MagII-D and MagII-L is similar to that of MagII-2 and MagII-3. Among all magnetite ores, MagII-2 has the lowest FeO content (85.06–91.45 wt%) and the highest SiO_2 content (1.03–4.43 wt%). The content of V_2O_3 is similar across MagII-1 (0–0.03 wt%), MagII-2 (0–0.04 wt%), and MagII-3 (0.01–0.04 wt%).

4.3. Trace Element Composition of Magnetite

The LA-ICP-MS results of five types of magnetite are presented in Supplementary Table S2. MagI has relatively lower W, Ta, Nb, Zn, Sr, Sn, Sb, Ga, Y, Zr (0.01–1 ppm), Mg, Ti, and Al (100–1000 ppm), while having relatively higher V, Cr, and Ni (100–10,000 ppm) than the element contents of MagII (Figure 9; the difference in content is mainly between one and three orders of magnitude). However, MagI-D has relatively higher concentrations of Zn, Cr, Ti, and Al, but lower contents of Mg, Sn, Sb, and V than MagI-L. The concentration of Sr and Ni in MagI varies, with small fluctuations, and some elements (Y and Zr) of MagI are below the detection limit.

The concentration of MagII displays similar trends, although with different degrees of enrichment. MagII-1 and MagII-3 are purer forms of magnetite than MagII-2, and their higher Fe content leads to lower trace element content compared to MagII-2.

MagII-2 has the highest Mg, Al, Si, Ca (1000–10,000 ppm), Ni, Ga, Sr, Y, and Sb (0.1–30 ppm) among MagII. The Cr (10–50 ppm) and W (~0.1–3000 ppm) components of MagII-1 are higher than of MagII-2 and MagII-3.

MagII-1 has transitional characteristics between MagI and MagII, which has the lowest content of Mg, Al, Si, Ca, Sr, Y (one order of magnitude lower than in MagII-2), Ni, Ga, and Sb (~10 ppm). MagII-2 has the lowest Cr (10–20 ppm) and W (1–100 ppm) content. The content of W in MagII magnetite is characterized by a large variance. The contents of V and Zn (10–100 ppm) in MagII magnetite are similar.

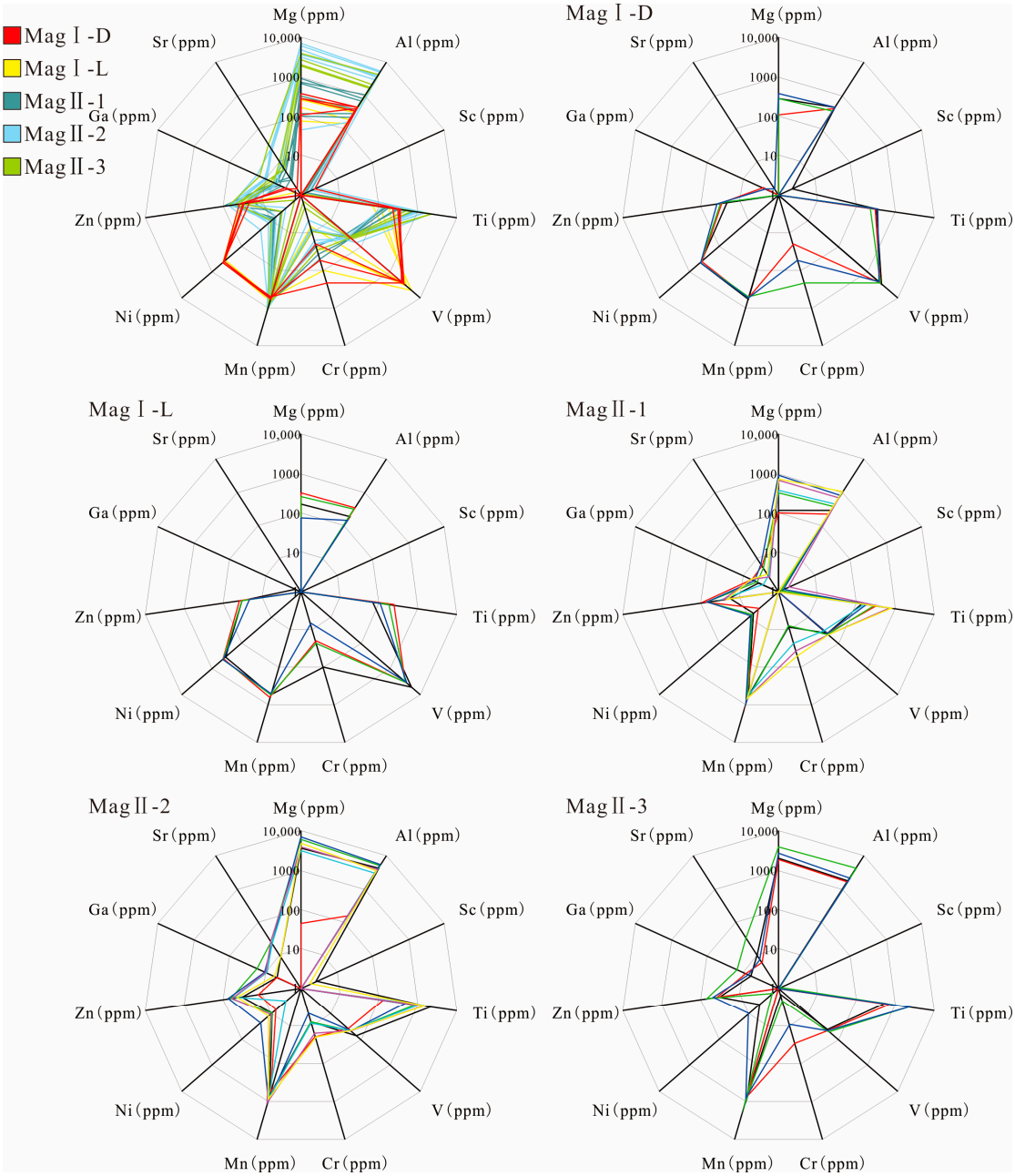

Figure 9. Radar plots of the upper threshold values, in parts per million, for the suite of important magnetite elements.

5. Discussion

5.1. Constrains on Texture and Composition of Magnetite

Magnetite (Fe_3O_4) has an inverse spinel structure with stoichiometry AB_2O_4, where A represents a divalent cation (Fe^{2+}) and B represents a trivalent cation (Fe^{3+}) [60,61]. Due to its mineral crystal structure characteristics, Fe^{2+} and Fe^{3+} iron elements can have a wide range of homomorphism. The replacement of trace elements in magnetite can reflect environmental changes during mineral formation [34,38]. The composition of magmatic magnetite is mainly controlled by the following conditions: (1) whole rock, magmatic, or fluid composition; (2) temperature; (3) pressure; (4) cooling rate: (5) oxygen fugacity; (6) sulfur fugacity; (7) Si activity [62–65].

According to the magnetite mineral classification and discrimination diagram (Figure 10) [37], the magnetite from Zhibo primarily falls within the categories of Kiruna, IOCG (iron oxide–copper–gold), skarn, and BIF (banded iron formation) deposits.

Consequently, our next step will involve examining the factors contributing to the occurrence of such a diverse range of magnetite types.

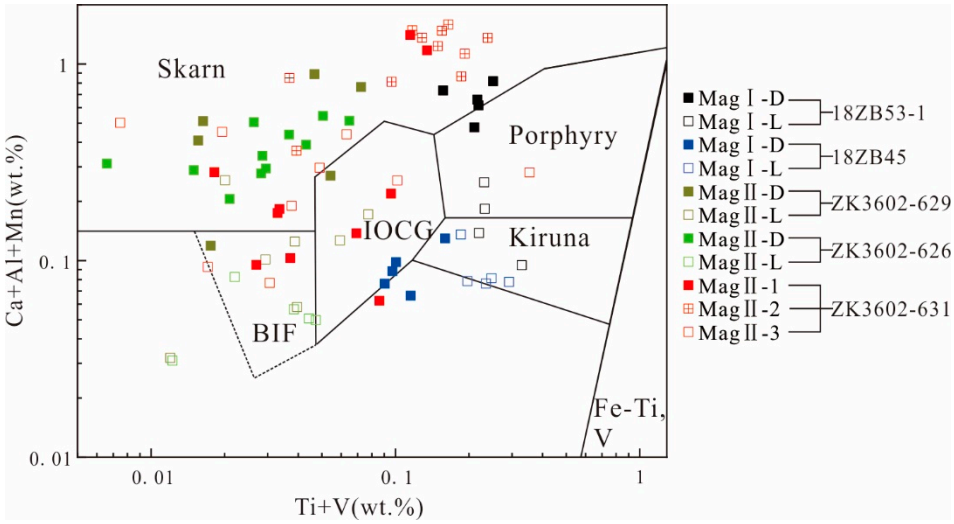

Figure 10. Plot of Ti + V vs. Ca + Al + Mn (wt%) in magnetite. Reference fields from [37].

Firstly, it is important to note that MagI-L shares the same Kiruna-type (IOA) origin as typical IOA deposits, but it differs slightly in composition. MagI-L is characterized by being a low-Ti magnetite, which sets it apart from typical volcanic magnetite. This variation in composition could be attributed to the influence of the host rocks' composition [34]. The low-Ti magnetite may be the result of the depletion of high-field strength elements in volcanic rocks in the deposit [9,10]. Furthermore, the composition of Zhibo magnetite could also be influenced by the low-Ti content in the initial fluid. This may result in minimal oxy-exsolution of Ti-rich oxides, which is a common feature of magnetite in igneous rocks [66].

Magnesium and vanadium are good indicators to distinguish magmatic and hydrothermal magnetite. Generally, hydrothermal magnetite contains higher Mg (>1000 ppm) and lower V (<1000 ppm), whereas magmatic magnetite is the opposite. The chemical behavior of Cr in magmatic and hydrothermal magnetite also tends to be enriched in magmatic magnetite [34,39].

MagI-L and MagI-D have similar characteristics as magmatic magnetites, such as low Mg (<400 ppm), high Cr, and high V (>2000 ppm) contents (Figure 9). MagI has a high V content and low Ti/V ratio (Figure 11), indicating that the magnetite formed under reducing fluid conditions. The ratio of Ti+V/Al+Mn can be used to distinguish between magmatic magnetite and hydrothermal magnetite, with values typically ranging from 0.1 to 0.5 considered characteristic of hydrothermal magnetite [34]. The mineral assemblage and the composition of the massive sulfide-free magnetite (MagI) support the origin of magmatic magnetite. In terms of texture, MagI-D differs significantly from MagI-L, and the characteristics of pores and irregular morphology in magnetite particles both indicate that the metallogenic system at that time was unstable (Figure 7a,b) [41].

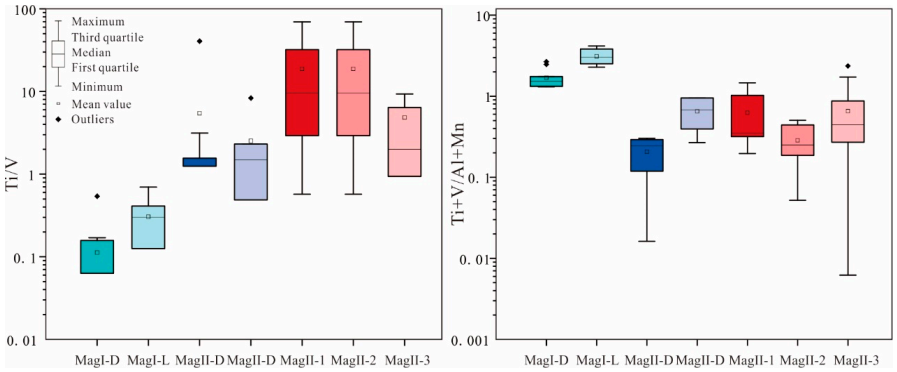

Figure 11. Boxplots of Ti/V and (Ti+V)/(Al+Mn) ratios.

Compared with MagII, Mag I exhibits more pure magmatic magnetite characteristics (Figure 12). Kiruna-type deposits can be distinguished from other deposits such as magmatic Fe–Ti–V-, porphyry-, and IOCG-type deposits by comparing V and Cr contents in the magnetite [45]. On the other hand, MagII displays the characteristics of hydrothermal magnetite. This observation further underscores that Zhibo magnetite possesses the attributes of multi-stage and multi-genesis formation. Because of the low-Ti volcanic rocks, V could act as a thermometer whose content is positively correlated with temperature [34]. From MagI-L to MagII-D, the decreasing content of V indicates a continuous decline in temperature.

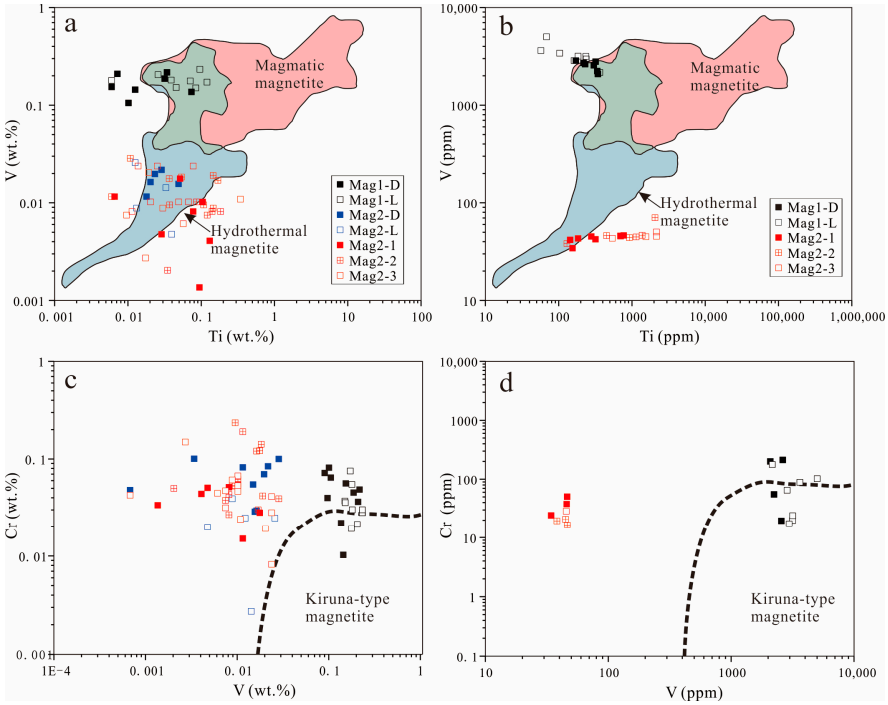

Figure 12. The concentration of Ti vs. V in magnetite. (**a**) EMPA; (**b**) LA-ICP-MS. The red area includes igneous-formed magnetite, while the blue area is defined by hydrothermal magnetite based on the data set of [40]. The data of MagI are plotted mostly in the overlapping area (green color), with some samples tending toward pure igneous magnetite. The concentration of V vs. Cr in magnetite. (**c**) EMPA; (**d**) LA-ICP-MS [45].

Therefore, we believe that MagI-L has the characteristics of high iron and low incompatible elements during the crystallization process of the original magma. The more magnetite crystallized from the original magma, the more incompatible elements will be enriched in the residual magma, resulting in the enrichment of incompatible elements in MagI-D crystallized at this stage. It is generally believed that IOCG and skarn are the genesis of hydrothermal deposits [67]. Some studies believe that IOA and IOCG deposits are

a single genetic continuum through a flotation model, wherein Mag I-D indicates its placement within the IOCG field (Figure 10) [31,68].

MagII from the ores containing sulfides coexists with similar mineral assemblages to hydrothermal magnetite [69]. Moreover, MagII has the chemical characteristics of hydrothermal magnetite (Figure 12). MagII-1 and MagII-2 have pores or voids, and the magnetite has distinct interfaces at different generations (Figure 7f). The evolving relationship between MagII-D and MagII-L is similar to that from MagII-2 to MagII-3, from skarn-type deposits to BIF. The trace element data of MagII-1 are mostly plotted in the same region as those of MagI-D in the Ca + Al + Mn vs. Ti + V diagram, indicating that it has a certain genetic inheritance relationship with MagI-D (Figure 10). At the same time, MagII exhibits the characteristics of hydrothermal magnetite (Figures 11 and 12). The dissolution–reprecipitation reaction is very common in the mineral metasomatic process in the hydrothermal system, and it can be distinguished by the following characteristics: (1) the outer form of the original mineral phase is preserved; (2) there is a distinct interface between the original mineral facies and the metasomatic mineral facies; (3) metasomatic minerals have good porosity; (4) there is a consistent crystallographic orientation between the original mineral facies and the metasomatic mineral facies [70,71]. The formation of MagII can be attributed to the change in physical and chemical parameters of the fluid and the dissolution–reprecipitation (DRP) reaction caused by the interaction of Mag-I crystals with the late fluid metasomatism.

The content of trace elements in hydrothermal magnetite is controlled by many factors and it is difficult to attribute such changes to a single physicochemical parameter. The multi-stage successive alteration can further complicate the magnetite geochemical composition [34,39]. Silicon, Mg, V, Ca, Al, and Mn could act as mobile elements during these processes.

Silicon could replace the tetrahedral site of magnetite crystals, being aware that the abundant inclusions in dark Mag may bias the measured amount of Si. The high Si content of the dark magnetite reflects the acidic ore-forming fluid that is not conducive to magnetite precipitation [33].

The vanadium content of magnetite is sensitive to oxygen fugacity (fO_2) and temperature during the DRP process. The vanadium content of magnetite is negative with fO_2, but positively correlated with temperature, which is consistent with the activity of Ti and Ga in the DRP process [32,39,72,73]. From MagII-1 to MagII-3, V and Ga contents have an increasing and then decreasing trend. It is characterized by an initial increase followed by a decrease in V and Ga concentrations, indicating that the temperatures are initially increased and then decreased and fO_2 is initially decreased and then increased [34,62,72]. The formation of MagII-1 and MagII-2 may be a process of increasing temperature due to the reactivation of the new magmatic–hydrothermal system, while the temperature from MagII-2 to MagII-3 gradually drops.

Based on this magnetite study, we believe that MagI-L represents magmatic magnetite. With the evolution of the original magma, MagI-D enriched with incompatible elements was formed. Then, magmatic magnetite was overprinted by multiple magmatic–hydrothermal alteration events to form hydrothermal magnetite.

5.2. Magmatic or Hydrothermal Origin

The Zhibo deposit has the characteristics of a magmatic affinity similar to the IOA deposit, such as the sharp contact between the ore body and wall rocks (Figure 4b), brecciated ores (Figure 4g), and flow structures (Figure 4j), which have been interpreted as evidence of magmatic origin [21,74,75]. The Zhibo deposit exhibits extensive late-stage hydrothermal alteration, characterized by significant epidotization during the transition from massive to disseminated ores (Figure 4a). Elevated content of sulfide and alteration assemblages are observed within the ores. These ore types have massive ores (Figure 4d,e), brecciated ores (Figure 4h), and banded ores (Figure 4i), which show obvious characteristics of a hydrothermal deposit [76,77].

In addition, there is dendritic magnetite in MagII (Figures 4e and 5d). This magnetite is widely developed in Kiruna and hydrothermal deposits. Previous studies have suggested that this magnetite is magmatic in origin, formed through rapid crystallization from immiscible iron–silicon melt [78] or degassed oxidative melt [79] during temperature decreases [80]. Multiple magmatic–hydrothermal fluids may have mixed with the magmatic fluid and consequently caused the undersaturation of iron in the fluids, leading to the dissolution of MagII-1 (high Fe and low Si, Al, and Ca concentrations) and re-precipitation of MagII-2 (low Fe and high Si, Al, and Ca), with significant porosity and abundant mineral inclusions. The incompatible elements in magnetite are discharged in the later re-equilibration process, which leads to the high Fe content in MagII-3 [42,64].

Along with the magmatic evolution, the magmatic fluid gradually reacted with the wall rock to form the hydrothermal magnetite and gangue [31,81]. Through a garnet U-Pb geochronology study, it has been confirmed that the AIMB has undergone at least three episodes of magmatic–hydrothermal activity [4]. Magmatic–hydrothermal activities led to multiple stages of skarn alteration, which resulted in the pre-formed minerals undergoing multi-stage alteration, thus creating a variety of ores types and magnetite textures.

Based on in situ iron isotope studies, the bimodal characteristics of Zhibo magnetite are identified [22]. It is argued that Zhibo magnetite is of magmatic and hydrothermal origin [22]. Combined with the study of magnetite in this paper, we argue that the Zhibo iron deposit was mainly formed by magmatic magnetite from an original iron-rich magma and then overprinted by hydrothermal mineralization.

6. Conclusions

Combining the field study and experimental analysis of the Zhibo iron deposit, one can observe that it has a variety of structural ores, such as massive, disseminated, banded, and brecciated. The contacts between the massive orebody and volcanic rock are sharp, while they are transitional between the disseminated orebody and epidotized wall rock. Field observations and laboratory studies revealed both magmatic and hydrothermal origin. There are two stages and seven types of magnetite in the Zhibo iron deposit. MagI-L crystallizes from the original magma, and MagI-D from the residual magma rich in incompatible elements. MagII has a core–mantle–rim texture, and MagII-1 is bright-colored magnetite rich in inclusions and pores. MagII-2 results from the metasomatism of MagII-1, forming magnetite with oscillatory zoning, but also containing inclusions. MagII-3 grows along MagII-2 and is bright-colored magnetite. MagII-L and MagII-D are similar to MagII-2 and MagII-3, but MagII-L and MagII-D do not have a core–mantle–rim texture. The chemical composition of MagII magnetite indicates its hydrothermal origin, but the difference in the chemical composition of magnetite in different generations reflects the change in temperature and fO_2. The formation of the Zhibo iron deposit has the characteristics of early magmatic genesis and late hydrothermal overprinting and has the characteristics of multi-stage mineralization.

Supplementary Materials: The following supporting information can be downloaded at: https://www.mdpi.com/article/10.3390/min14060548/s1, Table S1: EMPA results of different types of magnetite in the Zhibo iron deposit (wt.%); Table S2: La-ICP-MS results of different types of magnetite in the Zhibo iron deposit (ppm).

Author Contributions: Writing—original draft preparation, Y.W.; Writing—review and editing, P.S., H.F. and C.L. Investigation, J.Z., Y.L. and W.L. All authors have read and agreed to the published version of the manuscript.

Funding: This research is financially supported by the Key R&D Program of Xinjiang Uygur Autonomous Region (2023B03006), the National 305 Project Office of the People's Government of Xinjiang Uygur Autonomous Region and the "Tianchi Talent" Plan of Xinjiang Uygur Autonomous Region, and the National Key R&D Program of China (2018YFC0604004).

Data Availability Statement: The data presented in this study are available upon request from the corresponding author.

Acknowledgments: We are grateful for assistance during the fieldwork from the Bazhou Kaihong Mining Co., Ltd. of Xinjiang and the No. 3 Regional Geological Survey Party of Xinjiang Bureau of Geology and Mineral Exploration and Development.

Conflicts of Interest: The authors declare no conflict of interest.

References

1. Shen, P.; Pan, H.D.; Li, C.H.; Feng, H.X.; Wu, Y.; Shi, F.P.; Guo, X.C.; Li, W.G. Carboniferous ore-controlling volcanic apparatus and metallogenic models for the large-scale iron deposits in the Western Tianshan, Xinjiang. *Acta Petrol. Sin.* **2020**, *36*, 2845–2868. https://doi.org/10.18654/10000569/20200900. (In Chinese with English Abstract)
2. Zhu, Y.; Guo, X.; Song, B.; Zhang, L.; Gu, L. Petrology, Sr-Nd-Hf isotopic geochemistry and zircon chronology of the Late Palaeozoic volcanic rocks in the southwestern Tianshan Mountains, Xinjiang, NW China. *J. Geol. Soc.* **2009**, *66*, 1085–1099. https://doi.org/10.1144/0016-76492008-130.
3. Zhang, Z.; Hou, T.; Santosh, M.; Li, H.; Li, J.; Zhang, Z.; Song, X.; Wang, M. Spatio-temporal distribution and tectonic settings of the major iron deposits in China: An overview. *Ore Geol. Rev.* **2014**, *57*, 247–263. https://doi.org/10.1016/j.oregeorev.2013.08.021.
4. Yan, S.; Zhou, R.; Niu, H.; Feng, Y.; Nguyen, A.D.; Zhao, Z.; Yang, W.; Dong, Q.; Zhao, J. LA-MC-ICP-MS U-Pb dating of low-U garnets reveals multiple episodes of skarn formation in the volcanic-hosted iron mineralization system, Awulale belt, Central Asia. *GSA Bull.* **2019**, *132*, 1031–1045. https://doi.org/10.1130/b35214.1.
5. Li, C.; Shen, P.; Zhang, X.; Shi, F.; Feng, H.; Pan, H.; Wu, Y.; Li, W. Mineralogy and mineral chemistry related to the Au mineralization in the Dunde Fe-Zn deposit, western Tianshan. *Ore Geol. Rev.* **2020**, *124*, 103650. https://doi.org/10.1016/j.oregeorev.2020.103650.
6. Xiao, W.; Kusky, T. Geodynamic processes and metallogenesis of the Central Asian and related orogenic belts: Introduction. *Gondwana Res.* **2009**, *16*, 167–169. https://doi.org/10.1016/j.gr.2009.05.001.
7. Dong, L.H.; Feng, J.; Zhuang, D.Z.; Li, F.M.; Qu, X.; Liu, D.Q.; Tang, Y.L. Discussion of metallogenic models, mineralization characteristic and main type of rich iron ore of Xinjiang. *Xinjiang Geol.* **2012**, *29*, 416–422. (In Chinese with English Abstract)
8. Gao, J.; Long, L.L.; Klemd, R.; Qian, Q.; Liu, D.Y.; Xiong, X.M.; Su, W.; Liu, W.; Wang, Y.T.; Yang, F.Q. Tectonic evolution of the South Tianshan orogen and adjacent regions, NW China: Geochemical and age constraints of granitoid rocks. *Int. J. Earth Sci.* **2009**, *98*, 1221–1238. https://doi.org/10.1007/s00531-008-0370-8.
9. Zhang, X.; Tian, J.; Gao, J.; Klemd, R.; Dong, L.; Fan, J.; Jiang, T.; Hu, C.; Qian, Q. Geochronology and geochemistry of granitoid rocks from the Zhibo syngenetic volcanogenic iron ore deposit in the Western Tianshan Mountains (NW-China): Constraints on the age of mineralization and tectonic setting. *Gondwana Res.* **2012**, *22*, 585–596. https://doi.org/10.1016/j.gr.2011.06.007.
10. Luo, W.; Zhang, Z.; Duan, S.; Jiang, Z.; Wang, D.; Chen, J.; Sun, J.; Santosh, M. Geochemistry of the Zhibo submarine intermediate-mafic volcanic rocks and associated iron ores, Western Tianshan, Northwest China: Implications for ore genesis. *Geol. J.* **2018**, *53*, 3147–3172. https://doi.org/10.1002/gj.3243.
11. Yan, S.; Niu, H.C.; Zhao, J.X.; Bao, Z.W.; Sun, W.D. Ore-fluid geochemistry and metallogeny of the Dunde iron–zinc deposit in western Tianshan, Xinjiang, China: Evidence from fluid inclusions, REE and C–O–Sr isotopes of calcite. *Ore Geol. Rev.* **2018**, *100*, 441–456. https://doi.org/10.1016/j.oregeorev.2016.06.024.
12. Zhang, X.; Klemd, R.; Gao, J.; Dong, L.H.; Wang, X.S.; Haase, K.; Jiang, T.; Qian, Q. Metallogenesis of the Zhibo and Chagangnuoer volcanic iron oxide deposits in the Awulale Iron Metallogenic Belt, Western Tianshan orogen, China. *J. Asian Earth Sci.* **2015**, *113*, 151–172. https://doi.org/10.1016/j.jseaes.2014.06.004.
13. Sun, W.; Niu, Y.; Ma, Y.; Liu, Y.; Zhang, G.; Hu, Z.; Zhang, Z.; Chen, S.; Li, J.; Wang, X. Petrogenesis of the Chagangnuoer deposit, NW China: A general model for submarine volcanic-hosted skarn iron deposits. *Sci. Bull.* **2015**, *60*, 363–379. https://doi.org/10.1007/s11434-014-0684-9.
14. Yang, X.; Liang, T.; Guo, X.; Zheng, Y.; Zhou, Y.; Chen, Z.; Somerville, I.D. Mineralogy and stable isotope constraints on the genesis of submarine volcanic-hosted Beizhan iron deposit in the Western Tianshan, NW China. *Geol. J.* **2018**, *53*, 329–344. https://doi.org/10.1002/gj.3199.
15. Yang, X.; Mao, J.; Zhang, Z.; Robbins, L.J.; Planavsky, N.J.; Jiang, Z.; Duan, S.; Chen, Z. Episodic ferruginous conditions associated with submarine volcanism led to the deposition of a Late Carboniferous iron formation. *Geochim. Cosmochim. Acta* **2021**, *292*, 1–23. https://doi.org/10.1016/j.gca.2020.09.017.
16. Hou, T.; Zhang, Z.; Pirajno, F.; Santosh, M.; Encarnacion, J.; Liu, J.; Zhao, Z.; Zhang, L. Geology, tectonic settings and iron ore metallogenesis associated with submarine volcanism in China: An overview. *Ore Geol. Rev.* **2014**, *57*, 498–517. https://doi.org/10.1016/j.oregeorev.2013.08.007.
17. Huang, X.W.; Beaudoin, G. Textures and Chemical Compositions of Magnetite from Iron Oxide Copper-Gold (IOCG) and Kiruna-Type Iron Oxide-Apatite (IOA) Deposits and Their Implications for Ore Genesis and Magnetite Classification Schemes. *Econ. Geol.* **2019**, *114*, 953–979. https://doi.org/10.5382/econgeo.4651.
18. Knipping, J.L.; Fiege, A.; Simon, A.C.; Oeser, M.; Reich, M.; Bilenker, L.D. In-situ iron isotope analyses reveal igneous and magmatic-hydrothermal growth of magnetite at the Los Colorados Kiruna-type iron oxide-apatite deposit, Chile. *Am. Mineral.* **2019**, *104*, 471–484. https://doi.org/10.2138/am-2019-6623.

19. Xie, Q.; Zhang, Z.; Jin, Z.; Santosh, M.; Han, L.; Wang, K.; Zhao, P.; He, H. The high-grade Fe skarn deposit of Jinling, North China Craton: Insights into hydrothermal iron mineralization. *Ore Geol. Rev.* **2021**, *138*, 104395. https://doi.org/10.1016/j.oregeorev.2021.104395.
20. Tornos, F.; Velasco, F.; Hanchar, J.M. Iron-rich melts, magmatic magnetite, and superheated hydrothermal systems: The El Laco deposit, Chile. *Geology* **2016**, *44*, 427–430. https://doi.org/10.1130/g37705.1.
21. Tornos, F.; Velasco, F.; Hanchar, J.M. The Magmatic to Magmatic-Hydrothermal Evolution of the El Laco Deposit (Chile) and Its Implications for the Genesis of Magnetite-Apatite Deposits. *Econ. Geol.* **2017**, *112*, 1595–1628. https://doi.org/10.5382/econgeo.2017.4523.
22. Günther, T.; Klemd, R.; Zhang, X.; Horn, I.; Weyer, S. In-situ trace element and Fe-isotope studies on magnetite of the volcanic-hosted Zhibo and Chagangnuoer iron ore deposits in the Western Tianshan, NW China. *Chem. Geol.* **2017**, *453*, 111–127. https://doi.org/10.1016/j.chemgeo.2017.02.001.
23. Wang, Z.H.; Zhang, Z.H.; Jiang, Z.S.; Hong, W.; Tian, J.Q. Magnetite composition of Zhibo iron deposit in Western Tianshan Mountains and its genetic significance. *Miner. Depos.* **2012**, *31*, 983–998. (In Chinese with English Abstract)
24. Wang, Z.H.; Hou, L.; Gao, Y.W.; Zhang, Z.L.; Jiang, Z.S.; Zhang, Z.H. Geochemical characteristics and oxygen isotopes of magnetites in Zhibo iron deposit, Western Tianshan. *Acta Petrol. Sin.* **2018**, *34*, 2312–2326. (In Chinese with English Abstract)
25. Wang, Z.H.; Hou, L.; Gao, Y.W.; Zhang, Z.L.; Jiang, Z.S.; Zhang, Z.H. Chemical composition and sulfur isotope of pyrite from Zhibo iron ore deposit in Western Tianshan Mountains. *Miner. Depos.* **2018**, *37*, 176–193. (In Chinese with English Abstract)
26. Velasco, F.; Tornos, F.; Hanchar, J.M. Immiscible iron- and silica-rich melts and magnetite geochemistry at the El Laco volcano (northern Chile): Evidence for a magmatic origin for the magnetite deposits. *Ore Geol. Rev.* **2016**, *79*, 346–366. https://doi.org/10.1016/j.oregeorev.2016.06.007.
27. Larrañaga, A.; Briezewski, T.; Tornos, F.; de la Pinta, N.; Velasco, F. The relationship of destinezite to the acid sulfate alteration at the El Laco magnetite deposit, Chile. *Am. Mineral.* **2020**, *105*, 860–872. https://doi.org/10.2138/am-2020-7122.
28. Jiang, Z.; Zhang, Z.; Wang, Z.; Duan, S.; Li, F.; Tian, J. Geology, geochemistry, and geochronology of the Zhibo iron deposit in the Western Tianshan, NW China: Constraints on metallogenesis and tectonic setting. *Ore Geol. Rev.* **2014**, *57*, 406–424. https://doi.org/10.1016/j.oregeorev.2013.09.016.
29. Shcheka, S.A.; Platkov, A.V.; Vrzhosek, A.A.; Levashov, G.B.; Oktyabrsky, R.A. The trace element paragenesis of magnetite. *Nauka Mosc.* **1980**, *147*.
30. Wen, G.; Deng, X.-D.; Zhou, R.-J.; Duan, Z.; Cui, B.-Z.; Li, J.-W. Geology, geochronology and stable isotope studies at the Baijian Fe-(Co) skarn deposit, eastern China, with implications for ore genesis and regional Fe skarn metallogeny. *Ore Geol. Rev.* **2024**, *166*, 105935. https://doi.org/10.1016/j.oregeorev.2024.105935.
31. Rodriguez-Mustafa, M.A.; Simon, A.C.; del Real, I.; Thompson, J.F.H.; Bilenker, L.D.; Barra, F.; Bindeman, I.; Cadwell, D. A Continuum from Iron Oxide Copper-Gold to Iron Oxide-Apatite Deposits: Evidence from Fe and O Stable Isotopes and Trace Element Chemistry of Magnetite. *Econ. Geol.* **2020**, *115*, 1443–1459. https://doi.org/10.5382/econgeo.4752.
32. Canil, D.; Lacourse, T. Geothermometry using minor and trace elements in igneous and hydrothermal magnetite. *Chem. Geol.* **2020**, *541*, 119576. https://doi.org/10.1016/j.chemgeo.2020.119576.
33. Rojas, P.A.; Barra, F.; Reich, M.; Deditius, A.; Simon, A.; Uribe, F.; Romero, R.; Rojo, M. A genetic link between magnetite mineralization and diorite intrusion at the El Romeral iron oxide-apatite deposit, northern Chile. *Miner. Depos.* **2018**, *53*, 947–966. https://doi.org/10.1007/s00126-017-0777-x.
34. Nadoll, P.; Angerer, T.; Mauk, J.L.; French, D.; Walshe, J. The chemistry of hydrothermal magnetite: A review. *Ore Geol. Rev.* **2014**, *61*, 1–32. https://doi.org/10.1016/j.oregeorev.2013.12.013.
35. Bédard, É.; Hébert, R.; Guilmette, C.; Lesage, G.; Wang, C.S.; Dostal, J. Petrology and geochemistry of the Saga and Sangsang ophiolitic massifs, Yarlung Zangbo Suture Zone, Southern Tibet: Evidence for an arc–back-arc origin. *Lithos* **2009**, *113*, 48–67. https://doi.org/10.1016/j.lithos.2009.01.011.
36. Wen, G.; Li, J.-W.; Hofstra, A.H.; Koenig, A.E.; Lowers, H.A.; Adams, D. Hydrothermal reequilibration of igneous magnetite in altered granitic plutons and its implications for magnetite classification schemes: Insights from the Handan-Xingtai iron district, North China Craton. *Geochim. Cosmochim. Acta* **2017**, *213*, 255–270. https://doi.org/10.1016/j.gca.2017.06.043.
37. Dupuis, C.; Beaudoin, G. Discriminant diagrams for iron oxide trace element fingerprinting of mineral deposit types. *Miner. Depos.* **2011**, *46*, 319–335. https://doi.org/10.1007/s00126-011-0334-y.
38. McClenaghan, M.B. Indicator mineral methods in mineral exploration. *Geochem. Explor. Environ. Anal.* **2005**, *5*, 233–245. https://doi.org/10.1144/1467-7873/03-066.
39. Nadoll, P.; Mauk, J.L.; Hayes, T.S.; Koenig, A.E.; Box, S.E. Geochemistry of Magnetite from Hydrothermal Ore Deposits and Host Rocks of the Mesoproterozoic Belt Supergroup, United States. *Econ. Geol.* **2012**, *107*, 1275–1292. https://doi.org/10.2113/econgeo.107.6.1275.
40. Nadoll, P.; Mauk, J.L.; Leveille, R.A.; Koenig, A.E. Geochemistry of magnetite from porphyry Cu and skarn deposits in the southwestern United States. *Miner. Depos.* **2014**, *50*, 493–515. https://doi.org/10.1007/s00126-014-0539-y.
41. Yin, S.; Ma, C.; Robinson, P.T. Textures and high field strength elements in hydrothermal magnetite from a skarn system: Implications for coupled dissolution-reprecipitation reactions. *Am. Mineral.* **2018**, *102*, 1045–1056. https://doi.org/10.2138/am-2017-5913.
42. Hu, H.; Lentz, D.; Li, J.W.; McCarron, T.; Zhao, X.F.; Hall, D. Reequilibration Processes in Magnetite from Iron Skarn Deposits. *Econ. Geol.* **2014**, *110*, 1–8. https://doi.org/10.2113/econgeo.110.1.1.

43. Hu, X.; Chen, H.; Huang, X.; Zhang, W. Texture and composition of magnetite in the Duotoushan deposit, NW China: Implications for ore genesis of Fe–Cu deposits. *Mineral. Mag.* **2020**, *84*, 398–411. https://doi.org/10.1180/mgm.2020.29.
44. Knipping, J.L.; Bilenker, L.D.; Simon, A.C.; Reich, M.; Barra, F.; Deditius, A.P.; Lundstrom, C.; Bindeman, I.; Munizaga, R.J.G. Giant Kiruna-type deposits form by efficient flotation of magmatic magnetite suspensions. *Geology* **2015**, *43*, 591–594. https://doi.org/10.1130/G36650.1.
45. Knipping, J.L.; Bilenker, L.D.; Simon, A.C.; Reich, M.; Barra, F.; Deditius, A.P.; Wälle, M.; Heinrich, C.A.; Holtz, F.; Munizaga, R. Trace elements in magnetite from massive iron oxide-apatite deposits indicate a combined formation by igneous and magmatic-hydrothermal processes. *Geochim. Cosmochim. Acta* **2015**, *171*, 15–38. https://doi.org/10.1016/j.gca.2015.08.010.
46. Allen, M.B.; Windley, B.F.; Chi, Z. Paleozoic collisional tectonics and magmatism of the Chinese Tien-Shan, Central-Asia. *Tectonophysics* **1993**, *220*, 89–115. https://doi.org/10.1016/0040-1951(93)90225-9.
47. Windley, B.F.; Allen, M.B.; Zhang, C.; Zhao, Z.Y.; Wang, G.R. paleozoic accretion and cenozoic redeformation of the Chinese Tien-Shan-Range, Central-Asia. *Geology* **1990**, *18*, 128–131. https://doi.org/10.1130/0091-7613(1990)018<0128:Paacro>2.3.Co;2.
48. Xiao, W.J.; Han, C.M.; Yuan, C.; Sun, M.; Lin, S.F.; Chen, H.L.; Li, Z.L.; Li, J.L.; Sun, S. Middle Cambrian to Permian subduction-related accretionary orogenesis of Northern Xinjiang, NW China: Implications for the tectonic evolution of central Asia. *J. Asian Earth Sci.* **2008**, *32*, 102–117. https://doi.org/10.1016/j.jseaes.2007.10.008.
49. Qian, Q.; Gao, J.; Klemd, R.; He, G.Q.; Song, B.A.; Liu, D.Y.; Xu, R.H. Early Paleozoic tectonic evolution of the Chinese South Tianshan Orogen: Constraints from SHRIMP zircon U-Pb geochronology and geochemistry of basaltic and dioritic rocks from Xiate, NW China. *Int. J. Earth Sci.* **2009**, *98*, 551–569. https://doi.org/10.1007/s00531-007-0268-x.
50. Ge, S.; Zhai, M.; Safonova, I.; Li, D.; Zhu, X.; Zuo, P.; Shan, H. Whole-rock geochemistry and Sr-Nd-Pb isotope systematics of the Late Carboniferous volcanic rocks of the Awulale metallogenic belt in the western Tianshan Mountains (NW China): Petrogenesis and geodynamical implications. *Lithos* **2015**, *228–229*, 62–77. https://doi.org/10.1016/j.lithos.2015.04.019.
51. Kroner, A.; Kovach, V.; Alexeiev, D.; Wang, K.L.; Wong, J.; Degtyarev, K.; Kozakov, I. No excessive crustal growth in the Central Asian Orogenic Belt: Further evidence from field relationships and isotopic data. *Gondwana Res.* **2017**, *50*, 135–166. https://doi.org/10.1016/j.gr.2017.04.006.
52. Wang, B.; Liu, H.S.; Shu, L.S.; Jahn, B.M.; Chung, S.L.; Zhai, Y.Z.; Liu, D.Y. Early Neoproterozoic crustal evolution in northern Yili Block: Insights from migmatite, orthogneiss and leucogranite of the Wenquan metamorphic complex in the NW Chinese Tianshan. *Precambrian Res.* **2014**, *242*, 58–81. https://doi.org/10.1016/j.precamres.2013.12.006.
53. Chen, Y.C.; Liu, D.Q.; Tang, Y.L.; Wang, D.H.; Dong, L.H.; Xu, X.; Wang, X.D. *Mineral and Metallogenic Systems in Tianshan, China*; Geological Publishing House: Beijing, China, 2008.
54. Li, J.L.; Su, W.; Zhang, X.; Liu, X. Zircon Cameca U–Pb dating and its significance for granulite-facies granitic gneisses from the west Awulale Mountains, West Tianshan, China. *Geol. Bull. China* **2009**, *28*, 1852–1862. (In Chinese with English Abstract)
55. Feng, J.X.; Shi, F.P.; Wang, B.Y.; Hu, J.M.; Wang, J.T.; Tian, J.Q. *The Syngenetic Volcanogenic Iron Ore Deposits in Awulale Metallogenetic Belt Western Tianshan Mountains*; Geological Publishing House: Beijing, China, 2010. (In Chinese)
56. Tian, J.; Li, M.; Xie, R.S.; Peng, W.L.; Xie, W.B.; Yan, R.; Hu, C.J. *Resource Verified Reports of the Nuoerhu Iron deposit, Hejing County, Xinjiang*; No.3 Geological Brigade of Xinjiang Geology and Mineral Exploration and Development Bureau: Xinjiang, China, 2015; p. 214. (In Chinese)
57. Jiang, Z.; Wang, D.; Zhang, Z.; Duan, S.; Kang, Y.; Li, F. Application of in situ titanite U–Pb geochronology to volcanic-hosted magnetite deposit: New constraints on the timing and genesis of the Zhibo deposit, Western Tianshan, NW China. *Ore Geol. Rev.* **2018**, *95*, 325–341. https://doi.org/10.1016/j.oregeorev.2018.03.001.
58. Liu, Y.S.; Hu, Z.C.; Gao, S.; Gunther, D.; Xu, J.; Gao, C.G.; Chen, H.H. In situ analysis of major and trace elements of anhydrous minerals by LA-ICP-MS without applying an internal standard. *Chem. Geol.* **2008**, *257*, 34–43. https://doi.org/10.1016/j.chemgeo.2008.08.004.
59. Liu, Y.; Gao, S.; Hu, Z.; Gao, C.; Zong, K.; Wang, D. Continental and Oceanic Crust Recycling-induced Melt-Peridotite Interactions in the Trans-North China Orogen: U-Pb Dating, Hf Isotopes and Trace Elements in Zircons from Mantle Xenoliths. *J. Petrol.* **2009**, *51*, 537–571. https://doi.org/10.1093/petrology/egp082.
60. Fleet, M.E. The Structure of Magnetite. *Acta Crystallogr. Sect. B-Struct. Sci.* **1981**, *37*, 917–920. https://doi.org/10.1107/s0567740881004597.
61. Wechsler, B.A.; Lindsley, D.H.; Prewitt, C.T. crystal-structure and cation distribution in titanomagnetites (fe3-xtixo4). *Am. Mineral.* **1984**, *69*, 754–770.
62. Dare, S.A.S.; Barnes, S.-J.; Beaudoin, G. Variation in trace element content of magnetite crystallized from a fractionating sulfide liquid, Sudbury, Canada: Implications for provenance discrimination. *Geochim. Cosmochim. Acta* **2012**, *88*, 27–50. https://doi.org/10.1016/j.gca.2012.04.032.
63. Whalen, J.B.; Chappell, B.W.J.A.M. Opaque mineralogy and mafic mineral chemistry of I-and S-type granites of the Lachlan fold belt, southeast Australia. *Am. Mineral.* **1988**, *73*, 281–296.
64. Frost, B.R. Stability of oxide minerals in metamorphic rocks. *Rev. Mineral. Geochem.* **1991**, *25*, 469–488.
65. Ghiorso, M.S.; Sack, O. Fe-Ti oxide geothermometry: Thermodynamic formulation and the estimation of intensive variables in silicic magmas. *Contrib. Mineral. Petrol.* **1991**, *108*, 485–510.
66. Lindsley, D.H. Experimental studies of oxide minerals. *Rev. Mineral. Geochem.* **1991**, *25*, 69–106.

67. Verdugo-Ihl, M.R.; Ciobanu, C.L.; Cook, N.J.; Ehrig, K.; Slattery, A.; Courtney-Davies, L.; Dmitrijeva, M. Nanomineralogy of hydrothermal magnetite from Acropolis, South Australia: Genetic implications for iron-oxide copper gold mineralization. *Am. Mineral.* **2021**, *106*, 1273–1293. https://doi.org/10.2138/am-2021-7557.
68. Rodriguez-Mustafa, M.A.; Simon, A.C.; Bilenker, L.D.; Bindeman, I.; Mathur, R.; Machado, E.L.B. The Mina Justa Iron Oxide Copper-Gold (IOCG) Deposit, Peru: Constraints on Metal and Ore Fluid Sources. *Econ. Geol.* **2021**, *117*, 645–666. https://doi.org/10.5382/econgeo.4875.
69. Duran, C.J.; Barnes, S.-J.; Mansur, E.T.; Dare, S.A.S.; Bédard, L.P.; Sluzhenikin, S.F. Magnetite Chemistry by LA-ICP-MS Records Sulfide Fractional Crystallization in Massive Nickel-Copper-Platinum Group Element Ores from the Norilsk-Talnakh Mining District (Siberia, Russia): Implications for Trace Element Partitioning into Magnetite. *Econ. Geol.* **2020**, *115*, 1245–1266. https://doi.org/10.5382/econgeo.4742.
70. Putnis, A. Mineral replacement reactions: From macroscopic observations to microscopic mechanisms. *Mineral. Mag.* **2002**, *6*, 689–708. https://doi.org/10.1180/0026461026650056.
71. Putnis, A. Transient Porosity Resulting from Fluid–Mineral Interaction and its Consequences. *Rev. Mineral. Geochem.* **2015**, *80*, 1–23. https://doi.org/10.2138/rmg.2015.80.01.
72. Hu, X.; Xiao, B.; Jiang, H.; Huang, J. Magnetite texture and trace element evolution in the Shaquanzi Fe-Cu deposit, Eastern Tianshan, NW China. *Ore Geol. Rev.* **2023**, *154*, 105306. https://doi.org/10.1016/j.oregeorev.2023.105306.
73. Canil, D.; Grondahl, C.; Lacourse, T.; Pisiak, L.K. Trace elements in magnetite from porphyry Cu–Mo–Au deposits in British Columbia, Canada. *Ore Geol. Rev.* **2016**, *72*, 1116–1128. https://doi.org/10.1016/j.oregeorev.2015.10.007.
74. Hou, T.; Charlier, B.; Holtz, F.; Veksler, I.; Zhang, Z.; Thomas, R.; Namur, O. Immiscible hydrous Fe-Ca-P melt and the origin of iron oxide-apatite ore deposits. *Nat. Commun.* **2018**, *9*, 1415. https://doi.org/10.1038/s41467-018-03761-4.
75. Mungall, J.E.; Brenan, J.M.; Godel, B.; Barnes, S.J.; Gaillard, F. Transport of metals and sulphur in magmas by flotation of sulphide melt on vapour bubbles. *Nat. Geosci.* **2015**, *8*, 216–219. https://doi.org/10.1038/ngeo2373.
76. Li, W.; Xie, G.; Mao, J.; Zhu, Q.; Zheng, J. Mineralogy, Fluid Inclusion, and Stable Isotope Studies of the Chengchao Deposit, Hubei Province, Eastern China: Implications for the Formation of High-Grade Fe Skarn Deposits. *Econ. Geol.* **2019**, *114*, 325–352. https://doi.org/10.5382/econgeo.2019.4633.
77. Taofa, Z.; Mingan, W.; Yu, F.; Chao, D.; Feng, Y.; Lejun, Z.; Jun, L.; Bing, Q.; Pirajno, F.; Cooke, D.R. Geological, geochemical characteristics and isotope systematics of the Longqiao iron deposit in the Lu-Zong volcano-sedimentary basin, Middle-Lower Yangtze (Changjiang) River Valley, Eastern China. *Ore Geol. Rev.* **2011**, *43*, 154–169. https://doi.org/10.1016/j.oregeorev.2011.04.004.
78. Philpotts, A.R.; Doyle, C.D. Effect of magma oxidation-state on the extent of silicate liquid immiscibility in a tholeiitic basalt. *Am. J. Sci.* **1983**, *283*, 967–986. https://doi.org/10.2475/ajs.283.9.967.
79. Henriquez, F.; Martin, R.F. crystal-growth textures in magnetite flows and feeder dykes, El Laco, Chile. *Can. Mineral.* **1978**, *16*, 581–589.
80. Sillitoe, R.H.; Burrows, D.R. New field evidence bearing on the origin of the El Laco magnetite deposit, northern Chile. *Econ. Geol. Bull. Soc. Econ. Geol.* **2002**, *97*, 1101–1109. https://doi.org/10.2113/97.5.1101.
81. Barra, F.; Reich, M.; Selby, D.; Rojas, P.; Simon, A.; Salazar, E.; Palma, G. Unraveling the origin of the Andean IOCG clan: A Re-Os isotope approach. *Ore Geol. Rev.* **2017**, *81*, 62–78. https://doi.org/10.1016/j.oregeorev.2016.10.016.